Available online at www.sciencedirect.com
ScienceDirect
Journal of Power Sources 162 (2006) 727–734
JOURNAL OF POWER SOURCES
www.elsevier.com/locate/jpowsour

Electrodeposition synthesis and electrochemical properties of nanostructured γ-MnO_2 films

Shulei Chou, Fangyi Cheng, Jun Chen *

Institute of New Energy Material Chemistry, Nankai University, Tianjin 300071, PR China

Received 6 May 2006; received in revised form 9 June 2006; accepted 9 June 2006
Available online 26 July 2006

Abstract

The thin films of carambola-like γ-MnO_2 nanoflakes with about 20 nm in thickness and at least 200 nm in width were prepared on nickel sheets by combination of potentiostatic and cyclic voltammetric electrodeposition techniques. The as-prepared MnO_2 nanomaterials, which were characterized by scanning electron microscopy (SEM), transmission electron microscopy (TEM), X-ray diffraction (XRD), and X-ray photoelectron spectroscopy (XPS), were used as the active material of the positive electrode for primary alkaline Zn/MnO_2 batteries and electrochemical supercapacitors. Electrochemical measurements showed that the MnO_2 nanoflake films displayed high potential plateau (around 1.0 V versus Zn) in primary Zn/MnO_2 batteries at the discharge current density of 500 mA g^{-1} and high specific capacitance of 240 F g^{-1} at the current density of 1 mA cm^{-2}. This indicated the potential application of carambola-like γ-MnO_2 nanoflakes in high-power batteries and electrochemical supercapacitors. The growth process for the one- and three-dimensional nanostructured MnO_2 was discussed on the basis of potentiostatic and cyclic voltammetric techniques. The present synthesis method can be extended to the preparation of other nanostructured metal-oxide films.

Keywords: MnO_2; Nanostructures; Electrodeposition; Zn/MnO_2 battery; Supercapacitor

1. Introduction

Manganese dioxide (MnO_2) can form many kinds of polymorphs such as α-, β-, γ-, and δ-type, offering distinctive properties and wide applications as catalysts, ion-sieves, and especially as electrode materials in Li/MnO_2 and Zn/MnO_2 batteries [1–3]. Of all the MnO_2 structures, γ-MnO_2, which is usually produced by electrolytic method and thus called the synthetic electrolytic manganese dioxide (EMD), has better performance as an electrode material than that of the chemical manganese dioxide (CMD) in the battery industry. The γ-MnO_2 is predominantly used in aqueous Zn/MnO_2 cells which dominate the primary battery market segment and also in primary Li/MnO_2 cells [4,5]. On the other hand, MnO_2 appears to be a promising material of pseudocapacitor due to its superior electrochemical performance, environmentally friendly, and lower cost [6–10]. It is well-known that nanoscale materials exhibit peculiar and fascinating properties superior to their bulk counterpart. Electrode active materials with small crystalline particle size usually show high electrochemical activities and nice discharge performance due to their high specific surface areas. Furthermore, as the development of chemical and physical technologies, extensive interests have been focused on developing MnO_2 nanostructures and significant progress has been reported [11–24].

Up to now, there are mainly two methods in producing MnO_2 nanostructured materials, including hydrothermal method [11–16] and electrochemically deposited method [18–24]. The latter can be easily deposited on a substrate without further electrode preparation process. The thin-film preparation with electrodeposition can be divided into galvanostatic, potentiostatic (PS), pulsed current, pulsed potential, and cyclic voltammetric (CV) techniques according to the different styles of applied voltage or current [25]. For example, Hu et al. [21] reported on the hydrated MnO_x nanostructured films via a galvanostatic electrodeposition, showing the specific capacitance of 230 F g^{-1} measured from cyclic voltammetry at 25 mV s^{-1}. Wu's group [22] prepared the MnO_2 nanowire films using CV electrodeposition, displaying a high specific capacitance of 350 F g^{-1} under 0.1 mA cm^{-2} discharge rate. Ghaemi et al. [24] described that γ-MnO_2 nanowires made by employing a

* Corresponding author. Tel.: +86 22 23506808; fax: +86 22 23509118.
E-mail address: chenabc@nankai.edu.cn (J. Chen).

0378-7753/$ – see front matter © 2006 Elsevier B.V. All rights reserved.
doi:10.1016/j.jpowsour.2006.06.033

galvanostatic technique in the presence of surfactant showed enhanced rechargeability in alkaline Zn/MnO_2 batteries.

However, by using a single deposition technique, the morphologic variety of the product is limited. In addition, although the electrochemical methods are now and then applied to synthesize nanostructured manganese oxides, further applications of the obtained product are relatively scarce. Especially, advanced usage of MnO_2 nanomaterials is needed to investigate in Zn/MnO_2 batteries and electrochemical supercapacitors. In particular, it is still a challenge to develop the high rate discharge performance that is compatible with high power applications. Based on the above considerations, it is desirable to develop a simple, reliable, and reproducible technique for fabricating nanostructured γ-MnO_2 materials with different morphologies.

In this paper, we reported on the synthesis of γ-MnO_2 films with carambola-like nanoflakes by applying the combination of PS and CV. The as-obtained nanostructured films were directly used in primary alkaline Zn/MnO_2 batteries and electrochemical supercapacitors. The results showed that the γ-MnO_2 nanoflake films exhibited high potential plateau (around 1.0 V versus SCE) in primary Zn/MnO_2 batteries at the discharge current density of 500 mA g^{-1} and high specific capacitance of 240 F g^{-1} at the current density of 1 mA cm^{-2}.

2. Experimental

2.1. Nanostructured MnO_2 electrodeposition

The γ-MnO_2 nanostructured thin films were electrodeposited under room temperature with three electrode system. Prior to electrodeposition, the nickel sheets as working electrodes were polished to a smooth surface finish using successively finer grades of SiC paper, which was washed with distilled water, ethanol, and then dried under an air stream. A saturated calomel electrode (SCE) was used as the reference electrode, and graphite rod with high density and high surface area was used as the counter electrode. The electrolyte was composed of 0.1 M Na_2SO_4 and 0.1 M $Mn(CH_3COO)_2$ at pH 6.0, which was similar to that of Tench's experiment [18]. The electrochemical reaction of the manganese oxide formation occurs as Eq. (1) due to the decreasing pH value of electrolyte [25].

$$\begin{aligned} Mn^{2+} + 2H_2O &\rightarrow Mn^{(3+\Delta)} + (1 + \Delta)e^- \\ &\rightarrow MnO_2 + 4H^+ + 2e^- \end{aligned} \quad (1)$$

The MnO_2 thin films were prepared by using potentiostatic method under 0.6 V (SCE) for 15 min. The MnO_2 nanoflakes were synthesized by cycling for 15 min in combination of cyclic voltammetric technique in the potential range +0.60 V and +0.30 V (SCE) under the speed of 250 mV s^{-1} for 30 s and PS technique in the potential of 0.6 V (SCE) for 1.5 min. The MnO_2 naoflakes with the mass of 0.05 mg cm^{-2}, 0.1 mg cm^{-2}, and 0.2 mg cm^{-2} were obtained via combination of CV and PS techniques for 5 min, 15 min, 30 min, respectively.

2.2. Instrumental analyses

X-ray diffraction (XRD), X-ray photoelectron spectroscopy (XPS), scanning electron microscopy (SEM), and transmission electron microscopy (TEM) were used in characterizing the as-prepared MnO_2 nanomaterials. XRD analysis was carried out with a Rigaku INT-2000 X-ray generator. The X-ray intensity was measured over a diffraction 2-theta angle from 3° to 80° with a velocity of 0.02° $step^{-1}$ and 2° min^{-1}. The samples were also examined with XPS (ESCA-3400, Shimadzu Electron) using monochromatic Mg Kα radiation (1253.6 eV). The binding energy values were referenced to the carbon C 1s core peak at 284.7 eV. Specimens for SEM measurement were the nickel sheets with MnO_2 samples, which were attached to a SEM stub and then sputtered with a 2 nm layer of Pt. SEM images were taken from a JEOL JSM-6700 F Field Emission scanning electron microscope working at accelerating voltages of 5 kV or 10 kV. Samples for TEM analysis were directly electrodeposited onto the carbon-coated copper grids. TEM images were obtained with a Philips Tecnai F20 microscope working at an accelerating voltage of 200 kV.

Electrochemical measurements including cyclic voltammetry (CV), charge/discharge, and electrochemical impedance spectroscopy (EIS) were measured by a Parstat 2273 and an Arbin charge/discharge unit in an electrochemical cell. For Zn/MnO_2 batteries, the electrochemical cell contained samples on a nickel sheet as working electrode, a Zn sheet as counter electrode, a Hg/HgO as reference electrode, and 9 M KOH solution as the electrolyte. For MnO_2 electrochemical supercapacitors, the electrochemical cell contained samples on a nickel sheet as working electrode, a high surface carbon rod as counter electrode, a SCE as reference electrode, and 0.1 M Na_2SO_4 solution as the electrolyte. The discharge capacity/capacitance of the MnO_2 in the positive electrode was based on the amount of active material (MnO_2) excluding the weight of the nickel sheet.

3. Results and discussion

3.1. Characterization of MnO_2 nanostructured films

Using varied electrodeposition techniques can produce MnO_2 nanostructures with different morphologies, as shown by the SEM and TEM images of Fig. 1. Fig. 1a displays that MnO_2 nanoflakes with 20 nm in thickness and at least 200 nm in width were electrodeposited by the combination of CV and PS techniques. The as-prepared MnO_2 nanoflakes have similar structures with that of carambolas, an ornamental evergreen tree that is native to Southeast Asia with star-shaped ridged character (Fig. 1b). In situ TEM observation (Fig. 1c and d) was performed by directly electrodepositing MnO_2 onto carbon-coated copper grid using combination of CV and PS techniques. From Fig. 1c, it can be found that agglomerated nanoflakes with 10 nm in thickness are formed. In Fig. 1d, the HRTEM image shows the character of poor crystalline MnO_2. As a comparison, other two kinds of nanostructured MnO_2 thin films including nanoneedle films and nanorod films were also fabricated by single PS and CV techniques, respectively. Fig. 1e shows the SEM image of

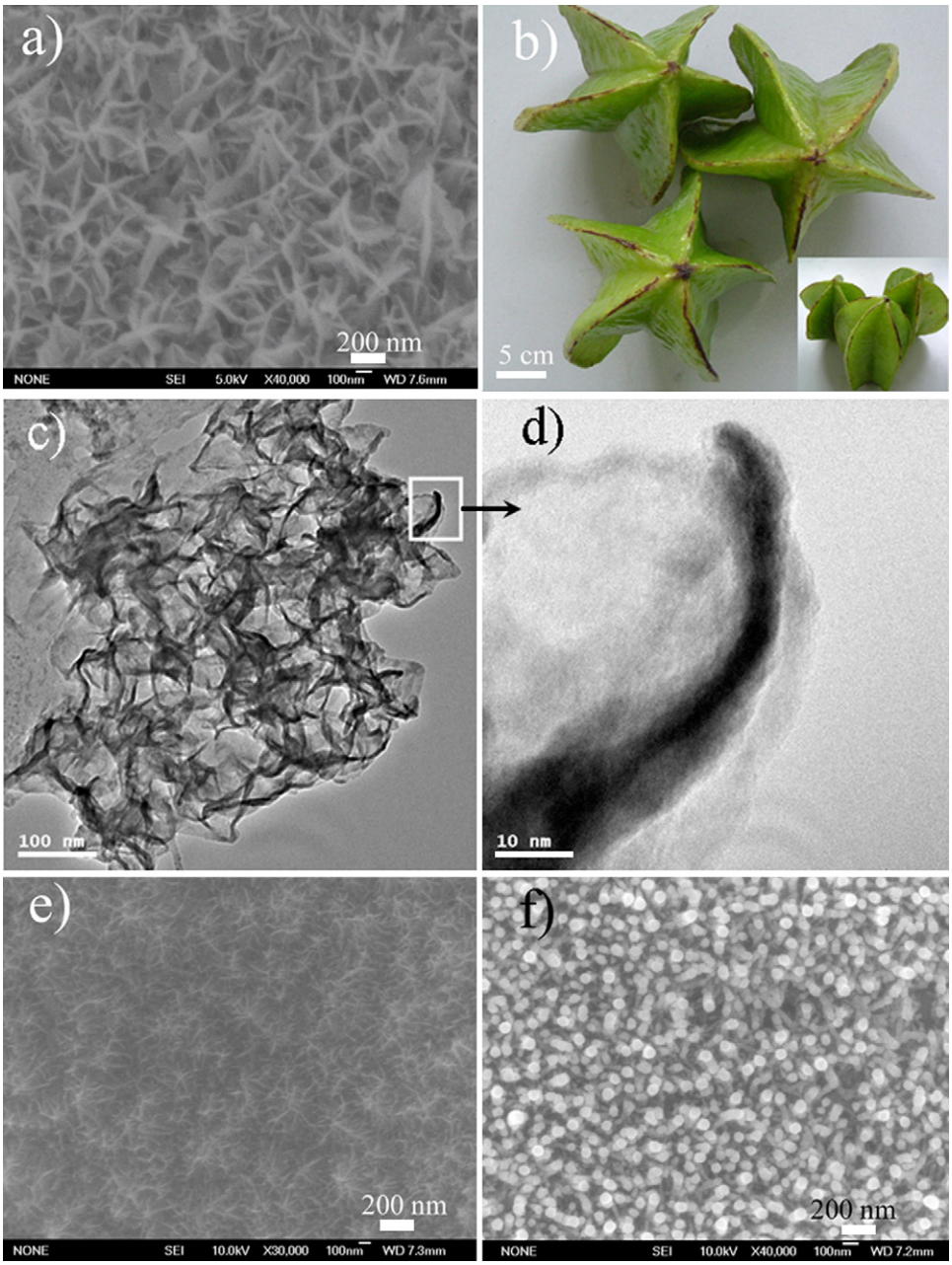

Fig. 1. Representative SEM (a) and TEM (c and d) images of γ-MnO_2 prepared by combined potentiostatic and cyclic voltammetric electrodeposition techniques; SEM images of γ-MnO_2 prepared by potentiostatic (e) and cyclic voltammetric (f) techniques; photograph of a kind of fruit called carambola native to Southeast Asia (b).

MnO_2 thin film electrodeposited by PS technique, indicating the formation of crossed needle-like nanostructures with 5–10 nm in diameters and 50–100 nm in lengths. Fig. 1f shows the top view of the oriented MnO_2 nanorod arrays with the diameters of 50–70 nm, which were electrodeposited by CV technique. The present nanorods are analogous to that reported by Wu et al. [22].

Fig. 2 shows the XRD patterns of the films that contain nanoneedles, nanorods, and nanoflakes, indicating the formation of γ-MnO_2 from the different electrodeposition techniques. Despite the low intensity and weakly crystalline nature, the diffraction peaks except that for Ni substrate can be ascribed to the crystal planes of (1 1 0), (0 2 1), and (0 6 1), confirming that the as-prepared products are γ-MnO_2 [4]. In addition, both the nanoflake and nanoneedle films exhibit better crystal structure than that of the nanorod films.

Fig. 3 shows the XPS spectra of the γ-MnO_2 films composed of nanoneedles, nanorods, and nanoflakes. The detected peaks appearing at the binding energy of 642.2 eV, which can be assigned to Mn $2p_{3/2}$, indicate that the element manganese of the three as-prepared samples is present in the chemical state of Mn^{4+}. The peak at the bonding energy of 654.4 eV, which corresponds to Mn $2p_{1/2}$, further confirms the sole existence of Mn^{4+} [26]. Furthermore, the quantitative XPS analysis demon-

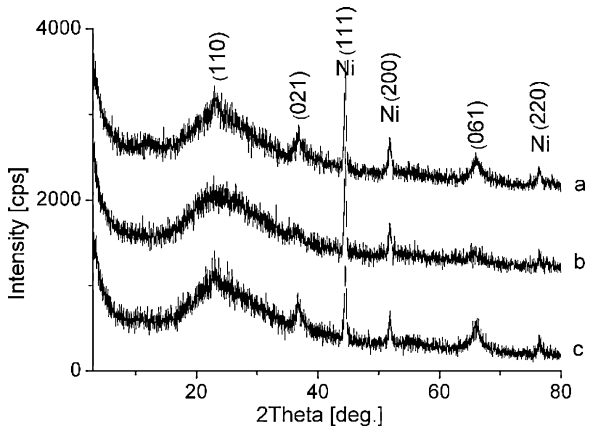

Fig. 2. XRD patterns of the films containing γ-MnO_2 nanoneedles (a), nanorods (b), and nanoflakes (c), electrodeposited on the Ni substrate by potentiostatic, cyclic voltammetric, and combined potentiostatic and cyclic voltammetric techniques, respectively.

strates that the atomic ratio of Mn to O is approximate to be 1:2, in good agreement with the XRD results.

3.2. *Zn/MnO_2 batteries*

Fig. 4 displays the cyclic voltammograms of the film electrodes containing γ-MnO_2 nanoneedles, nanorods, and nanoflakes at a scan rate of 10 mV s^{-1} under 20 °C. Reversible peaks are observed for all the three electrodes, but their characteristics are different to some extent. The experimental data of the voltammograms are summarized in Table 1. The related interpretation is as follows:

(1) When the electrodes were scanned cathodically, two peaks, namely the oxidation potential, E_O, and the oxygen-evolution potential, E_{OE}, appeared. During the following anodic scanning process, only one peak was observed, which was assigned to the reduction potential, E_R.
(2) The peak intensities of E_O, E_R, and E_{OE} for the nanostructured γ-MnO_2 film electrodes were in the order of nanorod > nanoflake > nanoneedle, that is, the corresponding reaction activities and energy densities also follow such sequence.
(3) The difference between the oxidation potential and the reduction potential, i.e. $E_O - E_R$, is taken as a measure of the reversibility of the electrode reaction. The smaller this value is, the more reversible the electrode reaction is. So the reversibility of the reaction between Mn^{4+} and Mn^{3+}, which takes place during electrode process as described below (Eq. (2)), is in the order of nanorods > nanoflakes > nanoneedles:

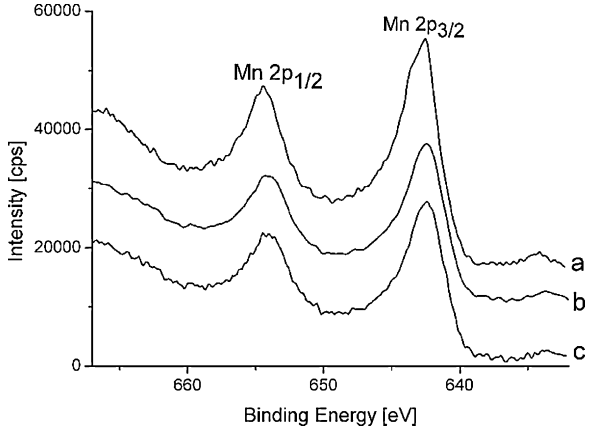

Fig. 3. XPS spectra of γ-MnO_2 films composed of nanoneedles (a), nanorods (b), and nanoflakes (c).

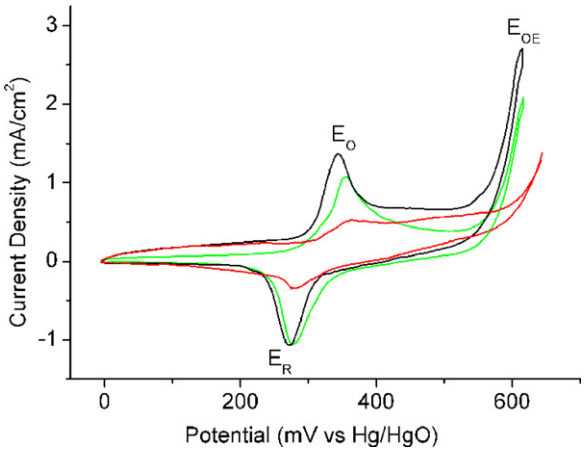

Fig. 4. Cyclic voltammograms of the film electrodes contained γ-MnO_2 nanoneedles (red line), nanorods (black line), and nanoflakes (green line) at a scan rate of 10 mV s^{-1} under 20 °C. "For interpretation of the references to color in this figure legend, the reader is referred to the web version of the article."

$$MnO_2 + H^+ + e \Leftrightarrow MnOOH \quad (2)$$

Fig. 5 shows the discharge curves of the γ-MnO_2 films composed of nanoneedles, nanorods, and nanoflakes at the discharge current density of 500 mA g^{-1} and the temperature of 20 °C. Because the γ-MnO_2 nanostructured films were directly used in the electrode measurement, that is, there are no electric additives adding into the nanostructures, the open-circuit potentials were as low as about 1.2 V. Table 2 shows the main feature of the discharge curves. It can be observed that the discharge plateau potentials are in the order of nanoflakes > nanorods > nanoneedles. Note that the nanorod electrode shows the highest specific capacity of 269 mAh g^{-1}, which is 87.3% of the theoretical specific capacity for transferring 1 mol electron from Mn^{4+} to Mn^{3+} by Eq. (3) [27]:

$$2MnO_2 + Zn + 2H_2O \rightarrow 2MnOOH + Zn(OH)_2 \quad (3)$$

Table 1
Experimental data summary from the cyclic voltammograms of the nanostructured γ-MnO_2 films

Electrodes	Potentials (mV)			
	E_R	E_O	E_{OE}	$E_O - E_R$
Nanoneedle film	279	362	642	83
Nanorod film	271	344	614	73
Nanoflake film	278	355	614	77

E_R: reduction potential; E_O: oxidation potential; E_{OE}: oxygen-evolution potential.

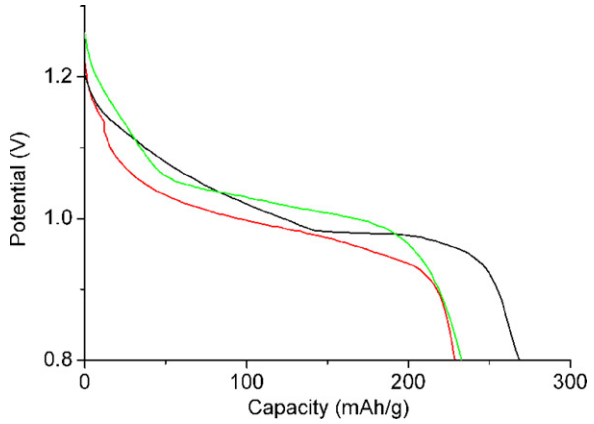

Fig. 5. Discharge curves of the film electrodes composed of nanoneedles (red line), nanorods (black line), and nanoflakes (green line) at 20 °C. The discharge current density is set at 500 mA g^{-1}. "For interpretation of the references to color in this figure legend, the reader is referred to the web version of the article."

3.3. Electrochemical supercapacitors

Fig. 6 shows the cyclic voltammograms of the γ-MnO_2 films of nanoneedles, nanorods, and nanoflakes at 20 °C and different scan rates (10 mV s^{-1}, 20 mV s^{-1}, 50 mV s^{-1}, and 100 mV s^{-1}). The main information of Fig. 6a–c was stated as follows:

(1) The nanoflake and nanorod films have higher capacitances than that of the nanoneedle films especially in lower cyclic rate (10 mV s^{-1}) due to the fact that both the nanoflake and the nanorod films have higher surface areas than that of the nanoneedle films.
(2) The nanoflake films have the largest area of cyclic voltammograms in higher scan rate (100 mV s^{-1}), which means that the nanoflake films have the best high power rate capacitance.
(3) The nanorod films have the best ideally cyclic voltammograms from higher to lower scan rate, indicating that the nanorod films have the best charge and discharge efficiency [22].

The specific capacitances and specific energies of γ-MnO_2 films with nanoneedles, nanoflakes, and nanorods at different current densities are summarized in Table 3. The main meanings are expressed below:

(1) The nanoflake films with a mass of 0.05 mg cm^{-2} have a highest specific capacitance up to 324 F g^{-1} under a current density of 0.1 mA cm^{-2}. That is, the thinnest film has the highest specific capacitance.
(2) The nanorod and nanoflake films with mass of 0.1 mg cm^{-2} have similar higher capacitances than that of the nanoneedle films, showing that higher surface ratio can provide the higher capacitance.
(3) The nanoflake films show the highest capacitance (240 F g^{-1}) under high rate discharge, being consistent with the CV test, in which the nanoflake films have the most ideal CV curve at high scan rate.

Table 2
Summary of the experimental data from the discharge measurement of the nanostructured film electrodes at 500 mA g^{-1} and 20 °C

Electrode	Discharge plateau potential (V)	Specific capacity (mAh g^{-1})	Specific energy (Wh kg^{-1})
Nanoneedle film	0.99	228	225.7
Nanorod film	0.98	269	263.6
Nanoflake film	1.02	233	237.7

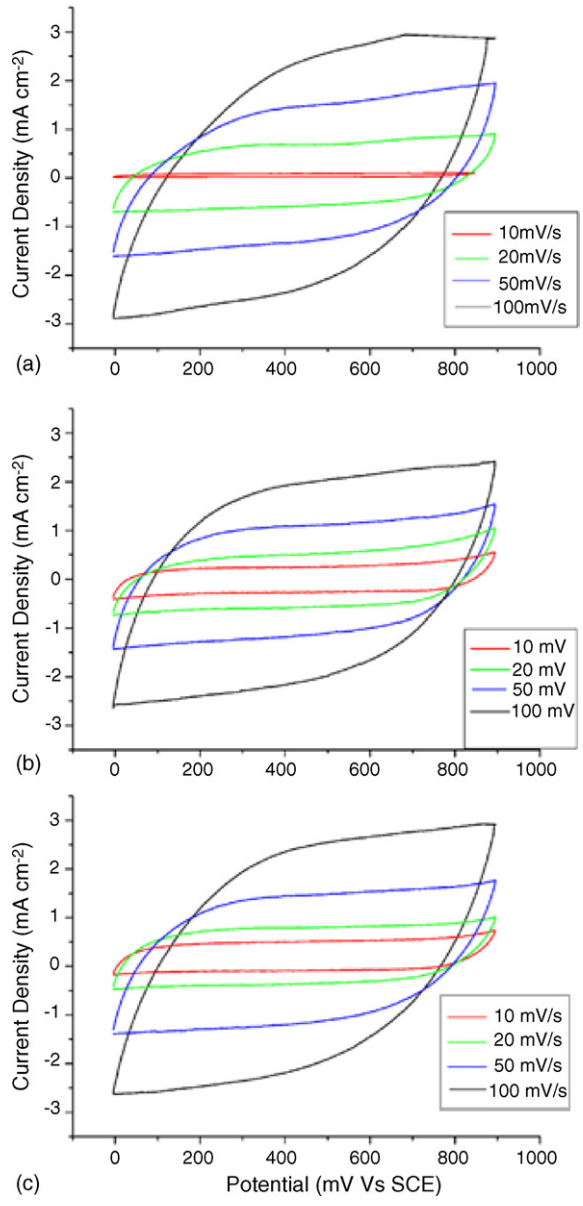

Fig. 6. Cyclic voltammograms of the γ-MnO_2 films with nanoneedles (a), nanorods (b), and nanoflakes (c) at 20 °C and in the scan rates of 10 mV s^{-1}, 20 mV s^{-1}, 50 mV s^{-1}, and 100 mV s^{-1}.

Fig. 7 shows typical charging and discharging curves of γ-MnO_2 nanoflake films with a mass of 0.2 mg cm^{-2} between 0 V and 0.9 V (SCE). The charge and discharge curves illustrate that

Table 3
Specific capacitance and specific energy of γ-MnO_2 films with nanoneedles, nanorods, and nanoflakes at the current densities of 0.1 mA cm^{-2}, 0.2 mA cm^{-2}, 0.5 mA cm^{-2}, and 1 mA cm^{-2}, and potential between 0 V and 0.9 V in 0.1 M Na_2SO_4 electrolyte at 20 °C

Sample	Mass of MnO_2 (mg cm^{-2})	Current density (mA cm^{-2})	Specific capacitance (F g^{-1})	Specific energy (Wh kg^{-1})
Nanoneedle films	0.1	0.1	258	29
		0.2	244	27
		0.5	213	24
		1	199	22
Nanorod films	0.1	0.1	289	33
		0.2	264	30
		0.5	241	27
		1	221	25
Nanoflake films	0.1	0.1	285	32
		0.2	278	31
		0.5	252	28
		1	240	27
Nanoflake films	0.05	0.1	324	36
		0.2	312	35
		0.5	300	34
		1	289	33
Nanoflake films	0.2	0.1	247	28
		0.2	216	24
		0.5	200	23
		1	188	21

γ-MnO_2 nanoflake films can be used as the ideal electrochemical supercapacitors.

Fig. 8 shows the Nyquist plots of γ-MnO_2 film electrodes with different morphologies from 10 kHz to 50 mHz. Three main aspects are listed as follows. Firstly, at very high frequencies, the intercept at real part *Zre* is almost the same, which means that the different morphologic electrodes have the same combination resistance of ionic resistance of electrolyte, intrinsic resistance of active materials, and contact resistance at the active material/current collector interface [28,29]. Secondly, the semicircle in the high frequency range associated with the surface

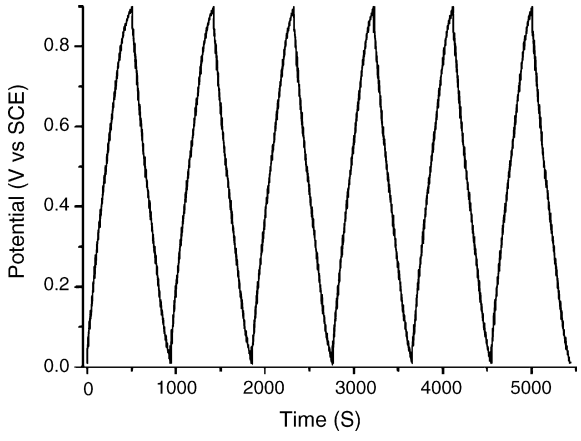

Fig. 7. Typical charging and discharging curves of γ-MnO_2 nanorod films with a mass of 0.2 mg cm^{-2} between 0 V and 0.9 V in 0.1 M Na_2SO_4 electrolyte at a current density of 0.1 mA cm^{-2}.

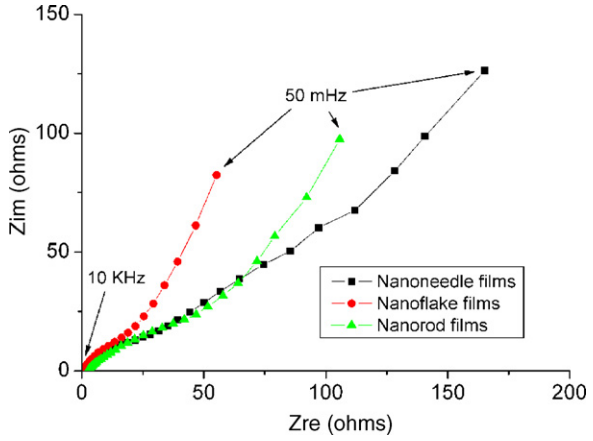

Fig. 8. Nyquist plots of γ-MnO_2 electrodes with the films of nanoneedles (square), nanoflakes (circle), and nanorods (triangle) from 10 kHz to 50 mHz.

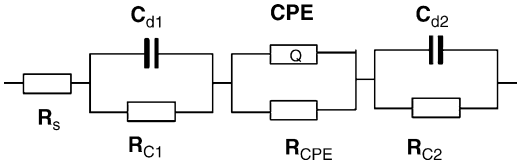

Fig. 9. The equivalent circuit of the EIS measurement shown in Fig. 8.

properties of porous electrode corresponds to the charge-transfer resistance. The charge-transfer resistance of the γ-MnO_2 films is in the order of nanoflakes < nanorods < nanoneedles. Finally, at the lower frequencies, an ideal capacitance shows a straight vertical line along the imaginary axis *Zim*. But in a real capacitor, this line usually has a finite slope to represent the diffusive resistance of electrolyte in electrode pores and the proton diffusion in host materials. Generally, this type of proton diffusion (solid-state diffusion) is slower in host materials like $Ni(OH)_2$ electrode [30] than that in electrolyte and the linearity is assumed to be the semi-infinite diffusion in solid materials. The slope of the diffusion line increases due to a lowered diffusion resistance.

EIS were also used to investigate the electrochemical active surface areas of the different morphologies [31]. The equivalent circuits shown in Fig. 9 can help us to calculate the electrochemical active surface area from the C_{d1} value using Eq. (4).

$$S_E = \frac{C_{d1}}{C_d} \quad (4)$$

where S_E is electrochemical active surface area, C_{d1} the double layer capacitance, and C_d is a constant capacitance of 20 μF cm^{-2} [32]. Table 4 summarizes the electrochemical active surface areas measured by EIS. The results showed that

Table 4
C_{d1} value and electrochemical active surface areas of nanorod, nanoneedle, and nanoflake films

Sample	C_{d1} (mF)	S_E (cm^2)
Nanorod	28.84	1442
Nanoneedle	1.984	100
Nanoflake	26.74	1337

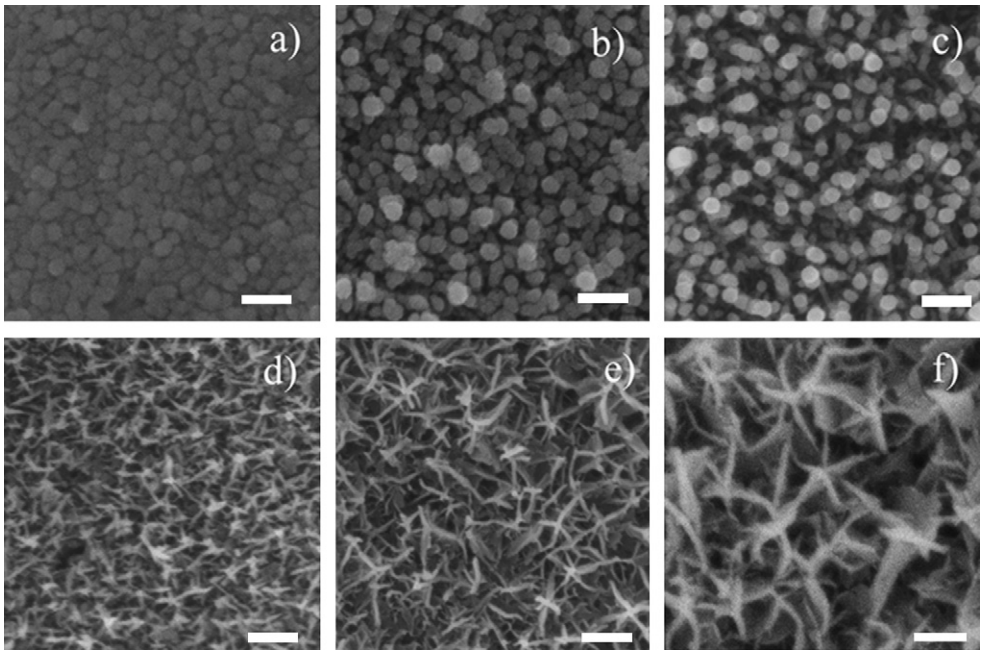

Fig. 10. SEM images of the obtained γ-MnO_2 films electrodeposited by CV technique for 30 s (a), 1.5 min (b), and 15 min (c). SEM images of γ-MnO_2 films electrodeposited by combination of CV and PS techniques for 2 min (d), 6 min (e), and 15 min (f). All the scale bars are 200 nm.

the electrochemical active surface areas were in the order of nanorods > nanoflakes > nanoneedles.

3.4. Mechanism of formation

In order to study the formation mechanism of γ-MnO_2 nanorods and nanoflakes, electrodeposition experiments for different deposition time were performed using CV technique and the combination of CV and PS techniques. Fig. 10a–c shows the SEM images of the obtained γ-MnO_2 nanostructures using CV technique electrodepositing for 30 s, 1.5 min, and 15 min, respectively. It can be seen in Fig. 10a that, in a short deposition time, spheres are formed and arranged compactly on the surface of the nickel substrate. In a longer reaction time, the deposited film becomes ragged, and some of the spheres are found to protrude out the surface (Fig. 10b). A sufficient deposition time of 15 min results in the formation of uniform nanorods (Fig. 10c) extending out the nickel substrate. Fig. 10d and e shows the SEM images of the electrodeposited films by applying combined CV and PS techniques for 2 min, 6 min, and 15 min, respectively. In Fig. 10d, both needle-like and flake-like nanostructures can be observed. With the time evolvement, the needle-like morphology disappears and the flakes become larger and larger to form network structures (Fig. 10f).

According to the above SEM observations, the present CV technique is favorable for the formation of 1D nanostructures, whereas the PS technique tends to result in 2D smooth surface structures. Combining the PS and CV techniques, 3D flake-network nanostructures with carambola-like structure were thereby achieved. The CV technique controls the velocity of the nucleation and crystal growth of MnO_2, leading to the anisotropic growth and resulting in 1D rod-like product that is perpendicular to the surface of the substrate. Under the PS condition, the crystal growth of MnO_2 is even and isotropic, favoring the formation of smooth structures along the surface of the substrate. Further studies are now underway to investigate the influence of electrodeposition parameters on the electrochemical performances of MnO_2 nanostructures, as well as to extend the present techniques to the synthesis of other nanostructures.

4. Conclusions

The γ-MnO_2 thin films with carambola-like nanoflakes were prepared on nickel sheets by combination of PS and CV electrodeposition techniques. Electrochemical measurements showed that γ-MnO_2 films with nanoflakes displayed higher potential plateau (around 1.0 V versus Zn) in primary Zn/MnO_2 batteries at the discharge current density of 500 mA g^{-1} and high specific capacitance of 240 F g^{-1} at the current density of 1 mA cm^{-2}. This work should foster the widespread application of electrolytic γ-MnO_2 nanostructures in both high-power batteries and electrochemical supercapacitors with improving the discharge plateau potential and the capacitance. In addition, the present CV and PS techniques can be extended to the research on electrodepositing other nanomaterials with controlled morphology and size.

Acknowledgements

This work was supported by the National NSFC, 973 Program, Ministry of Education, and Tianjin City Project.

References

[1] M.M. Thackeray, Prog. Solid State Chem. 25 (1997) 1–71.
[2] B. Ammundsen, J. Paulsen, Adv. Mater. 13 (2001) 943–956.

[3] M.S. Whittingham, Chem. Rev. 104 (2004) 4271–4301.
[4] Y. Chabre, J. Pannetier, Prog. Solid State Chem. 23 (1995) 1–130.
[5] M. Winter, R.J. Brodd, Chem. Rev. 104 (2004) 4245–4269.
[6] (a) S.C. Pang, M.A. Anderson, T.W. Chapman, J. Electrochem. Soc. 147 (2000) 444–4450;
(b) S.C. Pang, M.A. Anderson, J. Mater. Res. 15 (2000) 2096–2106.
[7] (a) H.Y. Lee, S.W. Kim, H.Y. Lee, Electrochem. Solid-State Lett. 4 (2001) A19–A22;
(b) M.S. Hong, S.H. Lee, S.W. Kim, Electrochem. Solid-State Lett. 5 (2002) A227–A230.
[8] S.F. Chin, S.C. Pang, M.A. Anderson, J. Electrochem. Soc. 149 (2002) A379–A384.
[9] (a) K.R. Prasad, N. Miura, Electrochem. Solid-State Lett. 7 (2004) A425–A428;
(b) K.R. Prasad, N. Miura, Electrochem. Commun. 6 (2004) 1004–1008.
[10] Y. Kuzuoka, C.J. Wen, J. Otomo, M. Ogura, T. Kobayashi, K. Yamada, H. Takahashi, Solid State Ionics 175 (2004) 507–510.
[11] (a) X. Wang, Y.D. Li, Chem. Commun. (2002) 764–765;
(b) X. Wang, Y.D. Li, J. Am. Chem. Soc. 124 (2002) 2880–2881.
[12] Y. Xiong, Y. Xie, Z. Li, C. Wu, Chem. Eur. J. 9 (2003) 1645–1651.
[13] C.Z. Wu, Y. Xie, D. Wang, J. Yang, T.W. Li, J. Phys. Chem. B 107 (2003) 13583–13587.
[14] Z.Y. Yuan, Z. Zhang, G. Du, T.Z. Ren, B.L. Su, Chem. Phys. Lett. 378 (2003) 349–353.
[15] V. Subramanian, H.W. Zhu, R. Vajtai, P.M. Ajayan, B.Q. Wei, J. Phys. Chem. B 109 (2005) 20207–20214.
[16] (a) F.Y. Cheng, J. Chen, X.L. Gou, P.W. Shen, Adv. Mater. 17 (2005) 2753–2756;
(b) F.Y. Cheng, J.Z. Zhao, W.E. Song, C.S. Li, H. Ma, J. Chen, P.W. Shen, Inorg. Chem. 45 (2006) 2038–2044.
[17] M. Sugantha, P.A. Ramakrishnan, A.M. Hermann, C.P. Warmsingh, D.S. Ginley, Int. J. Hydrogen Energy 28 (2003) 597–600.
[18] D. Tench, L.F. Warren, J. Electrochem. Soc. 130 (1983) 869–872.
[19] G.J. Moore, R. Portal, A.L.G. La Salle, D. Guyomard, J. Power Sources 97–89 (2001) 393–397.
[20] M. Ghaemi, Z. Biglari, L. Binder, J. Power Sources 102 (2001) 29–34.
[21] (a) C.C. Hu, C.C. Wang, J. Electrochem. Soc. 15 (2003) A1079–A1084;
(b) C.C. Hu, T.W. Tsou, Electrochim. Acta 47 (2002) 3523–3532.
[22] (a) M.S. Wu, Appl. Phys. Lett. 87 (2005), 153102–153102-3;
(b) M.S. Wu, J.T. Lee, Y.Y. Wang, C.C. Wan, J. Phys. Chem. B 108 (2004) 16331–16333.
[23] K. Katakura, S. Nishimura, Z. Ogumi, J. Power Sources 146 (2005) 217–221.
[24] M. Ghaemi, L. Khosravi-Fard, J. Neshati, J. Power Sources 141 (2005) 340–350.
[25] G.H.A. Therese, P.V. Kamath, Chem. Mater. 12 (2000) 1195–1204.
[26] J.F. Moulder, W.F. Stickle, P.E. Sobol, K.D. Bomben, in: J. Chastain (Ed.), Handbook of X-Ray Photoelectron Spectroscopy, Perkin-Elmer Corporation, Wellesley, MA, 1992.
[27] D. Linden, T.B. Reddy, Handbook of Batteries, third ed., McGraw-Hill, New York, 2002.
[28] J. Gamby, P.L. Taberna, P. Simon, J.F. Fauvarque, M. Chesneau, J. Power Sources 101 (2001) 109–116.
[29] P. Kurzweil, H.-J. Fischle, J. Power Sources 127 (2004) 331–340.
[30] F.Y. Cheng, J. Chen, P.W. Shen, J. Power Sources 150 (2005) 255–260.
[31] M. Mastragostino, A. Missiroli, F. Soavi, J. Electrochem. Soc. 151 (2004) A1919–A1924.
[32] A. Hamelin, T. Vitanov, E. Sevastyanov, A. Popov, J. Electroanal. Chem. 145 (1983) 225–264.